

Crater Detection Using Unsupervised Algorithms and Convolutional Neural Networks

Ebrahim Emami¹, Touqeer Ahmad, George Bebis, Ara Nefian, and Terry Fong

Abstract—Craters are among the most abundant features on the surface of many planets with great importance for planetary scientists. They reveal chronology information about planets and may be used for autonomous spacecraft navigation and landing. Although numerous research efforts have been carried out in the field of crater detection, existing crater detection algorithms (CDAs) are only helpful in a limited number of applications. A promising crater detection approach involves two main steps: 1) hypothesis generation (HG) and 2) hypothesis verification (HV). During HG, potential crater locations are detected. The validity of the hypothesized crater locations is then tested in a HV step. In this context, we discuss some commonly used algorithms for HG such as highlight-shadow region detection and Hough transform as well as our novel and enhanced algorithms based on interest point detection and convex grouping. A key objective of this paper is to analyze their performance while paying special attention to how they affect the accuracy of the verification step. To deal with different size craters, we focus on multiscale HG. For HV, we have chosen convolutional neural networks which have recently achieved state-of-the-art performance in many computer vision applications. Due to the variation of test sets in the literature, it is often challenging to compare the performance of different CDAs in a fair way. In this paper, we present a comprehensive performance evaluation and comparison of CDAs. Each algorithm has been trained/tested using common data sets generated by a systematic approach.

Index Terms—Convex grouping, convolutional neural networks (CNNs), crater detection.

I. INTRODUCTION

THE amount of data obtained from the moon, mars, and other planetary surfaces has been constantly increasing by new exploratory missions. Craters are among the main topographic features available on these surfaces created by the impact of meteoroids. As the main application of crater detection, accumulated numbers of craters and their size-frequency distribution provide the primary mechanism in studying chronology of planetary surfaces and their geological processes. Craters also provide significant landmarks for terrain-based navigation systems and have been used in applications such as accurate spacecraft landing, navigation, and control [1]–[4].

Manuscript received July 30, 2018; revised November 25, 2018; accepted January 30, 2019. Date of publication March 18, 2019; date of current version July 22, 2019. This work was supported by National Aeronautics and Space Administration Established Program to Stimulate Competitive Research under Grant NNX11AM09A. (Corresponding author: Ebrahim Emami.)

E. Emami, T. Ahmad, and G. Bebis are with the Department of Computer Science and Engineering, University of Nevada, Reno, Reno, NV 89577 USA (e-mail: ebrahim@nevada.unr.edu).

A. Nefian and T. Fong are with the Intelligent Robotics Group, NASA Ames Research Center, Moffett Field, CA 94035 USA.

Color versions of one or more of the figures in this paper are available online at <http://ieeexplore.ieee.org>.

Digital Object Identifier 10.1109/TGRS.2019.2899122

It is clear that the analysis of the huge planetary data available demands some sort of automation. Despite significant amount of work in crater detection, there exist no standard and generally acceptable tool for automatic crater detection. In practice, accurate crater detection is challenging due to variations in size, level of degradation, internal morphologies, and imaging parameters. Overlapping craters or other geological features may also bring difficulties in automatic crater detection [5].

Numerous automatic crater detection approaches have been proposed in the past. These algorithms detect craters using supervised, unsupervised, or a combination of both techniques. Although many of these algorithms have only been tested on a limited data set, they have also been used as the basis to improve lunar and planetary crater catalogs [6]–[9]. Recent advances in the field of computer vision and machine learning have motivated the investigation and development of more effective crater detection algorithms (CDAs). In this paper, we investigate CDAs based on the combination of fast unsupervised techniques and advanced supervised deep neural network classifiers. Similar to other object detection applications, such as vehicle detection [10], we consider a two-step detection process, consisting of a multiscale hypothesis generation (HG) step and a hypothesis verification (HV) step. In the HG step, the candidate crater regions are hypothesized using unsupervised and fast image processing techniques. The resultant hypotheses are then provided to the HV step for verification. We have investigated four HG algorithms in this paper based on Hough transform [11], highlight-shadow regions [12], convex grouping [13], and interest points [14]. The performance of the HG algorithms and their impact on the HV step have been analyzed using extensive experiments. HV is essentially a two-class pattern classification problem between crater and noncrater classes. In this paper, convolutional neural networks (CNN), which have recently achieved state-of-the-art performance in many computer vision applications, have been investigated for HV. In particular, the performance of three CNN architectures for crater classification has been investigated in an effort to improve HV performance. A systematic approach for creating and augmenting a crater detection training set has also been considered along with a study on the effects of the training set to the HV performance.

This paper has its origin in NASA's Crater Detection Challenge [15] with the eventual goal of providing information on planetary formation and geology, along with applications in landing site selection, and rover path planning and navigation. Although we have targeted the detection of specific size craters (i.e., 10–100-m radius) on lunar surface, due to the greater

importance of small craters in planetary science applications, the findings of this research provides insights for small crater detection on similar planetary surfaces.

To our knowledge, this paper presents the most comprehensive evaluation and improvements of HG approaches. First, we have proposed a novel and effective CDA based on interest point detection. Second, the performance of our convex grouping-based CDA has been significantly improved compared to the original algorithm proposed in [16]. Third, the Hough transform and highlight-shadow region-based HG algorithms, inspired from popular crater detection approaches, have been included in our evaluation. Using a common data set has allowed us to perform a fair performance evaluation and comparison of these algorithms. The evaluation of the brute-force (i.e., sliding-window) approach further demonstrates the benefits of the two-step HG and HV approach.

This paper is an extension of [16] with some major improvements and extensions. First, we have improved some of the HG algorithms (i.e., convex grouping) investigated in [16] and added new ones (i.e., interest points) which have shown the best overall performance. Second, we have performed additional experiments by introducing new training sets where instead of choosing the training samples randomly, we chose them from the hypotheses generated using the HG algorithms. This has yielded more performance improvements compared to using random training sets. Finally, three CNN architectures were evaluated in this paper compared to only one CNN in [16]. Moreover, we have experimented with different parameters such as using rectified linear unit (ReLU) activation functions in this paper compared to sigmoid activation functions in [16].

The rest of this paper is organized as follows. Section II summarizes previous work. In Section III, the details of the CDAs investigated are explained. Our experimental results and discussion are presented in Section IV. Finally, Section V presents our conclusions and future research directions.

II. BACKGROUND

A large number of CDAs have been proposed in the literature including in more than 70 publications reviewed in [3]. In this section, we discuss the most recent and major work.

Unsupervised CDAs are a major part of previous work on crater detection. Assuming some intuitive visual characteristics for craters, unsupervised algorithms employ image processing and pattern recognition techniques to locate these features. For instance, by assuming circular rims for craters, techniques like Hough transform have been customized to detect such regions. Variations of the Hough transform have been among the most popular techniques to detect craters as circular features. Troglia *et al.* [17] employed a generalized Hough transform to detect the center of crater regions; these points are then used as seeds for watershed segmentation to detect the actual crater regions. Galloway *et al.* [18] used Hough transform to verify regions which are manually extracted from images. Bue and Stepinski [19] employed Hough transform to detect candidate crater regions on binary curvature maps computed from Martian DEMs. Candidate regions are then verified based on criteria on crater rim pixel distributions.

Honda *et al.* [20] have also evaluated the effect of several preprocessing techniques on the performance of crater detection based on the Hough transform.

Salamuniccar and Lončarić [21] employed fuzzy Hough transform for crater detection on Martian DEMs which improves performance by taking into account the gradient value and orientation of edges. The detected circles are verified based on probabilities computed from several crater morphological criteria, and the final craters parameters are fine tuned. This CDA was later successfully employed in [22] to detect craters on DEMs reconstructed from lunar optical images. Other circle detection approaches such as tensor voting [23] or genetic algorithms [20] have also been used for crater detection.

In a pioneer automated crater detection work, Banderia *et al.* [24] detected craters by analyzing the probability volume obtain from template matching-based algorithm. The volume is particularly calculated from the template matching of circular crater templates in the possible range of radiuses with the extracted edge images. Assuming convex groups of edges for crater rims, candidate crater region detection based on convex grouping is proposed by Emami *et al.* [16]. Highlight and shadow regions of craters have also been used as the main features for crater detection. Smirnov [25] detected crater highlight and shadow regions based on thresholding and analysis of edge shapes. Urbach and Stepinski [12] considered highlight and shadow features as an indicator of possible crater regions. The extracted features are then filtered using, power, area, and shape filters. The remaining highlight and shadow features are then matched to detect candidate regions. As it can inferred from previous works, unsupervised approaches alone cannot be used for accurate crater detection and the hypotheses generated by these algorithms need to be verified, typically using supervised techniques.

Stepinski *et al.* [26] employed decision trees for the verification of candidate regions which are detected using a flooding-based algorithm from enhanced digital elevation models (DEM). Decision trees work based on craters' morphological attributes such as diameter, depth, and elongation. Urbach and Stepinski [12] used moments and other simple shape features to represent image patches which are classified as crater and noncrater using decision trees. Savage *et al.* [27] presented a parametric model to characterize small craters based on morphological features such as diameter, rim height, and eccentricity on imagery and elevation modes of Martian surface using a Bayesian approach. The model is then utilized to distinguish between primary and secondary small craters.

Haar-like features have also been extensively used in the literature for crater region classification [28]–[30]. Emami *et al.* [31] studied the application of various feature descriptors in combination with support vector machines (SVMs) for crater region classification. As in many other computer vision applications, CNNs have also been employed for automatic crater detection in recent years. Cohen *et al.* [32] applied a CNN on already extracted image patches from a crater detection data set. Emami *et al.* [16] also employed a CNN to classify regions

Algorithm 1

- 1- Negate the input image (I) to obtain the negative image (N).
- 2- Remove large features from both images using:

$$I = I - MI$$

$$N = N - MN$$

where MI and MN are smoothed images obtained by median filtering of I and N respectively.

- 3 - Update the input image by combining I and N :

$$I = I + N$$

- 4 - Apply a Gaussian filter G on I at multiplescales toobtain smoothed images $I_1, I_2, \text{ and } I_3$.

-Perform steps 5-8 on images $I_1, I_2, \text{ and } I_3$:

- 5 - Detect edges using Canny edge detector.
- 6 - Perform line fitting on the detected edges.
- 7 - Extract convex group of lines.
- 8 - Find the enclosing boundingbox B_c around each detected convex group.
- 9 - Combine overlapping detections (B_s)

extracted by convex grouping. Palafox *et al.* [33] used CNNs to detect other planetary features such as volcanic rootless cones (VRCs) and transverse aeolian ridges (TARs) on martian images. They employ five different size networks trained for each class of VRCs and TARs. A sliding window is applied on the test images to feed regions to the CNNs.

III. AUTOMATIC CRATER DETECTION

In this section, we provide details about the crater detection approaches considered in this paper based on multiscale HG and HV using CNNs.

A. Multiscale Hypothesis Generation

The goal of HG is the detection of possible crater regions using fast image processing techniques in order to avoid classifying the whole image. For this purpose, we consider prior assumptions about the appearance of craters. Specifically, we look for convex groups of edges, circular groups of edges, highlight and shadow regions, and groups of interest points. In Sections III-A1–III-A4, each of these algorithms is explained.

1) *HG Using Convex Grouping*: Algorithm 1 detects convex groups of edges as candidate crater locations. This algorithm is based on our original algorithm proposed in [16] with modifications that lead to significant performance improvements.

In steps 1–3, large image features in the image are removed using a median filter of size 101. To detect various sized craters, multiscale Gaussian filtering is performed in step 4 using

$$G(x, y) = \frac{1}{2\pi\sigma^2} e^{-\frac{x^2+y^2}{2\sigma^2}} \quad (1)$$

where (x, y) represents a sample pixel location.

Algorithm 2

- 1- Apply median filter on input.
- 2 - Apply the Gaussian filter G on I at multiple scales to obtain smoothed images $I_1, I_2, \text{ and } I_3$.
- Perform steps 3-5 on each image $I_1, I_2, \text{ and } I_3$:
 - 3 - Detect edges using Canny edge detector.
 - 4 - Apply Hough Circle Transform.
 - 5 - Find the enclosing bounding box B_c around each detected circle.
- 6 - Combine overlapping detections (B_s)

Steps 5–8 apply convex grouping to generate a preliminary set of hypotheses. The split-and-merge algorithm [34] has been used to fit lines on the detected edges in step 6. These line segments are characterized by direction, orientation, and length. Convex groups of lines are then detected using the technique propose by Jacobs [13]. Based on the convex grouping technique, a set of oriented lines form a convex shape, if for each line segment, all the other line segments lie on the same side as its normal. The algorithm only detects the most salient convex groups. A convex group of lines is salient if

$$\frac{L_{1,n}}{L_{1,n} + G_{1,n}} > k \quad (2)$$

where $L_{1,n}$ represents the sum of lengths of all the line segments (l_i) in group, $G_{1,n}$ represent sum of gap lengths (G_i) in the group, and k is predefined threshold. The algorithm starts by considering every line segment as a convex group, and then expand the groups by adding additional line segments using backtracking [13].

Any of the proposed HG algorithms might detect multiple regions corresponding to a single crater. Multiple detections slow down HV and result in a larger number of false detections. Step 9 removes such detections using two substeps. First, the detected regions are clustered based on an intersection over union (IOU) criterion which is computed as

$$\text{IOU}(B_i, B_j) = \frac{\text{Area}(B_i \cap B_j)}{\text{Area}(B_i \cup B_j)} \quad (3)$$

where B_i, B_j are two sample rectangular regions. B_i and B_j are clustered together if $\text{IOU}(B_i, B_j)$ is greater than a predefined threshold. In the second substep, each cluster of boxes is represented by a box whose sides are the average width and height.

2) *HG Using Hough Transform*: The HG algorithm based on Hough transform is straightforward. This algorithm generates hypotheses by applying Hough circles transform on multiscale edge images as follows.

Noise reduction is a key step for robust Hough transform results. In Algorithm 2, median filtering first and then multiscale Gaussian filtering perform this job. The circular Hough transform [11] is then applied followed by the next steps similar to Algorithm 1.

3) *HG Using Highlight-Shadow Region Detection*: Craters typically consist of matching pairs of highlight and shadow regions. This assumption is a key factor for the next HG

Algorithm 3

- 1- Negate the input image (I) to obtain the negative image (N).
- 2- Remove large features of both images using:

$$\begin{aligned} I &= I - MI \\ N &= N - MN \end{aligned}$$

where MI and MN are smoothed images obtained by median filtering of I and N respectively.

- 3 - Apply thresholding on I and N .
- 4 - Extract connected components C_I and C_N from I and N and respectively.
- 5 - Find the enclosing bounding box b_i for each $c_i \in C_I$ and b_j for each $c_j \in C_N$; call them B_I and B_N respectively.
- 6 - Match the pairs of highlight ($b_i \in B_I$) and shadow ($b_j \in B_N$) regions when:

$$\text{distance}(b_i, b_j) < 2 \times \text{sqrt}(\max(\text{area}(b_i), \text{area}(b_j))) \quad (4)$$

- 7 - Find the enclosing bounding box B_c around each paired region and the remaining unpaired regions.
- 8 - Combine overlapping detections (B_s).

algorithm. This algorithm is inspired from the CDA proposed in [12], and consists of the following steps.

The main goal of steps 1–4 is the extraction of highlight and shadow regions in the original (I) and negative (N) images. The first two steps are similar to Algorithm 1 and their goal is to remove large image features. Prior to the connected component extraction in step 4, small regions are filtered using morphological opening. In step 6, a highlight (b_i) and shadow (b_j) region are matched if the Euclidean distance between the center points of these boxes is less than the distance computed in (4). This threshold is relative to the size of the larger region and is obtained empirically. In the case of a match, the minimum enclosing box containing the matched boxes is considered as the new hypothesized location. The previous steps do not guarantee the extraction of both highlight and shadow regions for each crater, especially for eroded craters. To avoid missing such craters, the remaining unmatched regions are also added to the final set of hypotheses in step 7.

4) *HG Using Interest Points*: Craters often have strong intensity variations in multiple directions. This characteristic is the key factor for the next HG algorithm based on the Shi–Tomasi corner detector [14]. To detect interest points, for each pixel p , neighborhood $N(p)$ is considered and a covariance matrix is computed over $N(p)$ as

$$M = \begin{bmatrix} \sum_{N(p)} \left(\frac{dI}{dx}\right)^2 & \sum_{N(p)} \left(\frac{dI}{dx} \times \frac{dI}{dy}\right) \\ \sum_{N(p)} \left(\frac{dI}{dx} \times \frac{dI}{dy}\right) & \sum_{N(p)} \left(\frac{dI}{dy}\right)^2 \end{bmatrix} \quad (5)$$

where (dI/dx) and (dI/dy) are the derivatives in x - and y -direction computed using the Sobel operator. The

Algorithm 4

- 1- Create an image pyramid by down-sampling the input four times: $\{I_1, I_2, I_3, I_4\}$
- For each image I_i in the image pyramid perform steps 2-4:
 - 2- Calculate matrix M (equation 5) for every pixel in the image, and store the minimum eigenvalues.
 - 3- Threshold the stored eigenvalues (equation 6) to detect the interest points.
 - 4- Generate a box B_c of size 10×10 around each interest point.
- 5- Upscale the detections (B_s)
- 6- Combine overlapping detections (B_s)

eigenvalues of M are then computed and the minimum eigenvalue λ_{\min} is stored for each pixel. To select the interest points, the stored eigenvalues are compared to an empirically obtained threshold which is computed as

$$\lambda_{\min} + (\lambda_{\max} - \lambda_{\min})/10 \quad (6)$$

where λ_{\min} and λ_{\max} are the minimum and maximum eigenvalues computed over all image pixels. The HG algorithm using interest points consists of the following steps.

The image pyramid is built by subsampling the input image by a factor of 2 at each level. As a result, the resulted detections are also scaled by the same factor. In particular, in step 5, we upscale each box by a factor of 2^l , where l is the level where the interest point was detected at. It should be mentioned that interest points were first used for crater detection in [35] although using a different approach. Our implementation of that approach resulted in very poor results which prompted us to develop the modified approach presented in Algorithm 4.

B. CNNs for Crater Region Verification

The set of hypothesized craters typically contain a large number of false detections which must be removed in the HV step. In this paper, we have only considered CNNs for HV as they have outperformed traditional classification methods (e.g., SVMs) in [16].

Unlike conventional approaches involving feature extraction and classifier training, CNNs learn both the features and classification model during training. In this way, they reduce the need of designing optimal preprocessing, feature extraction, and classification techniques to obtain the best classification results. Here, we analyze the performance of three different CNN architectures for crater HV. These networks are named $\text{CNN}_{15}\text{C}_2\text{F}_1$, $\text{CNN}_{32}\text{C}_2\text{F}_1$, and $\text{CNN}_{32}\text{C}_2\text{F}_3$. In each of the names, the size of the input image is represented by the subscript of CNN, while the number of convolutional layers and fully connected layers are represented by the subscripts of C and F, respectively. The CNN architectures are illustrated using the feature maps in Fig. 1. Next, we explain these architectures in more detail.

1) $\text{CNN}_{15}\text{C}_2\text{F}_1$: This network is inspired from the CNN proposed in [32]. The input layer is fed with images of size 15×15 , followed by two convolutional layers involving the

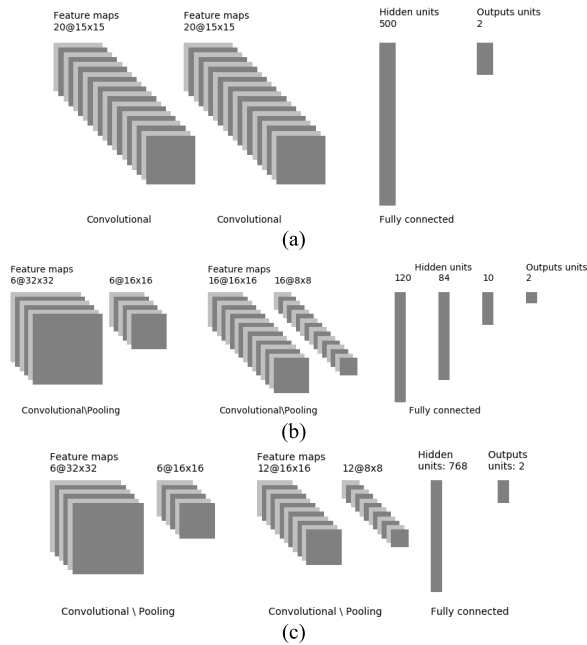


Fig. 1. Convolutional/pooling and fully connect layer's feature maps of (a) $CNN_{15}C_2F_1$, (b) $CNN_{32}C_2F_3$, and (c) $CNN_{32}C_2F_1$ networks.

application of 20 kernels of size 5×5 . A fully connected layer involving 500 neurons follows the second convolutional layer. Although kernels of size 4×4 were used in [32], the kernel size was changed to 5×5 in this paper based our validation set experiments.

2) $CNN_{32}C_2F$: This network is based on the popular LeNet [36] and received images of size 32×32 as input. The next two layers consist of convolutional and max pooling modules where the convolutional layers consist of 6 and 16 kernels of size 5×5 , respectively. Three fully connected layers of sizes 120, 84, and 10 neurons follow the convolutional layers.

3) $CNN_{32}C_2F_1$: This network, which is also LeNet based and has been motivated by our earlier work [16], is applied on images of size 32×32 . The input layer is followed by a convolutional and max pooling module, with six convolutional filters of size 5×5 . A similar module with 12 convolutional filters and a fully connected layer with 768 neurons make the rest of the network.

All three CNNs outputs are calculated through soft-max functions. Also, the outputs of all layers are passed through ReLUs which have shown better performance compared to other activation functions. The max-pooling operations in the networks are obtained using 2×2 filters.

IV. EXPERIMENTAL RESULTS

A. Data Set

Our crater detection data set consists of 578 images of size 600×400 with a resolution of 1 meter per pixel obtained from the Lunar Reconnaissance Orbiter Narrow Angle Cameras. Each image has tens of craters with a radius in the range of 10–100 m which have been confirmed by multiple NASA citizen scientists. Our algorithms have been designed to detect craters within this size range, although in practice smaller

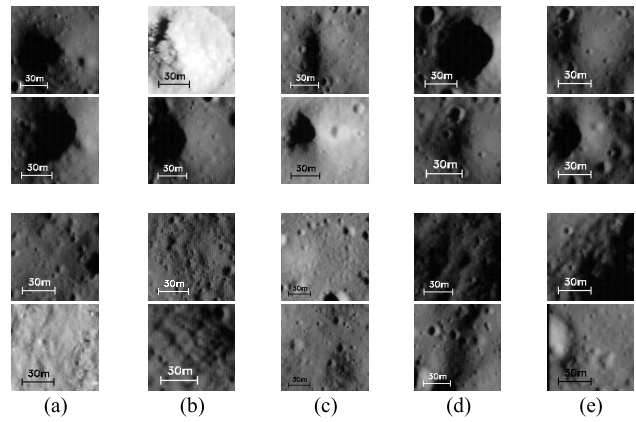


Fig. 2. (Top) Positive and (Bottom) negative samples using (a) randomly extracted image patches, (b) Hough transform, (c) highlight-shadow region detection, (d) convex grouping, and (e) interest points.

craters are also often detected. We have randomly chosen 400 images from the data set for training purposes while the rest are kept for testing. In order to train and evaluate the performance of our algorithms, several data sets have been extracted from each set of images.

1) *Training Set 1, Randomly Chosen Image Patches*: The positive training samples of this data set are extracted around the labeled craters. Data augmentation is used to increase the variation of the training data. In particular, the labeled regions are slightly mislocalized by resizing them or applying translations in random directions. The transformed regions maintain at least 50% overlap with the original regions. The negative samples are extracted randomly from noncrater regions in the training images. Using this approach, 7600 samples of each class are extracted. The final training set contains 6600 samples of each class while the rest of the samples are kept for validation purposes.

2) *Training Set 2, Hypothesized Image Patches*: This data set consists of four mutually exclusive training sets. To produce each set, one of the four HG algorithms is applied on the training images. The hypothesized regions are then manually checked and labeled as crater or noncrater regions. Each of the four training sets was generated by randomly selecting 6600 samples of each class from the hypothesized regions. Sample image patches from Training Set 1, and four parts of Training Set 2 are shown in Fig. 2.

3) *Test Set 1, Randomly Chosen Image Patches*: Similar to the approach used to generate Training set 1, this test set is generated by extracting 3500 positive and negative samples from the original test.

4) *Test Set 2, Fully Labeled Images*: Test set 2 contains 20 images randomly selected from the original set of test images. As mentioned earlier, although our algorithms are adjusted to detect craters with radius larger than 10 m, smaller craters are also often detected. For a fair comparison, smaller regions which are detected by our algorithms are not counted as true or false positives. Therefore, to estimate the number of false positives correctly, smaller size craters need to be labeled too. In our experiments, hundreds of various size craters were manually labeled in each test image, and used

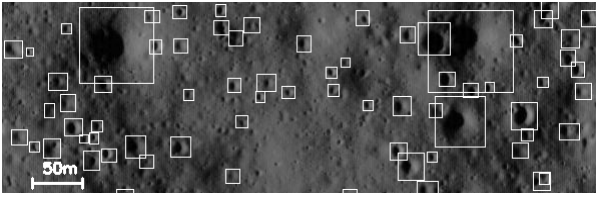


Fig. 3. Sample test site with all labeled craters shown in white.

as ground truth to test all combinations of the HG and HV algorithms. Fig. 3 shows a sample test region with all labeled craters shown in white.

B. Evaluation Criteria

To evaluate crater detection performance, we need to define a criterion for true detections. A hypothesis is considered a true positive if its IOU with ground truth is at least 30%; otherwise, it is considered a false positive. The choice of the threshold was motivated from an earlier “crater detection” NASA challenge [15]. The recall and precision rates are used to evaluate performance

$$\text{Recall} = \frac{TP}{GP} \times 100, \quad \text{Precision} = \frac{TP}{TP + FP} \times 100 \quad (7)$$

where TP, FP, and GP are the number of true positives, false positives, and ground truth craters, respectively.

Additional criteria are needed to evaluate the performance of the HG algorithms. For instance, although hypothesized regions with more than 30% IOU with ground truth are considered true, more accurate localization is desired. Therefore, the average IOU between ground truth and the generated hypotheses is reported.

Furthermore as mentioned earlier, multiple hypotheses might correspond to the same crater. However, hypothesized regions with higher IOU have a better chance to be verified which leads to an overall better performance. Therefore, the average IOU between ground truth and the highest overlapping hypotheses is also reported for each HG algorithm.

Finally, the average number of hypotheses per image is reported for each HG algorithm. Less number of hypotheses is desirable since it lowers the computational load of the HV step and leads to less false detections overall.

C. Performance Evaluation of HG Algorithms

In this section, we analyze the performance of the HG algorithms on Test Set 2. Table I summarizes the results of these experiments. As shown in the first row of Table I, all HG algorithms achieve close to perfect recall rate in detecting true craters. This due to designing these algorithms and fine-tuning their parameters with the goal of achieving a high recall rate at the expense of more false positives. This is desirable because while it is possible to reject false positives in the HV phase, false negatives cannot be recovered in that phase.

In order to show the effectiveness of the two phase crater detection scheme based on HG and HV compared to the brute force approach, we have also employed a sliding window approach for HG. The second column in Table I illustrates the

performance of this approach. Similar to other HG algorithms, we have adjusted the sliding window parameters to obtain near to perfect recall rate. Specifically, the window moves over the image by a stride half its size and a scale factor of 2. Although a finer set of parameters could be used, the chosen parameters resulted a recall rate of 99.61% while generating only 2813 hypothesis for each image. For obvious reasons, the sliding window approach generates hypotheses having the lowest average IOU (41.20%) with the ground truth. It is interesting to note that due to the high number of hypotheses generated, the best hypothesized regions have a relatively high IOU (56.64%) with ground truth.

The next column in Table I summarizes the performance of the Hough transform-based HG. Achieving a 99.61% recall rate, this algorithm generates a relative large number of hypotheses per image (i.e., 773). The detected crater hypotheses have an average IOU of 47.96% with ground truth, while the highest overlapping detections have an IOU of 60.76% with ground truth. These IOU results are relatively high compared to the other algorithms, ranking Hough transform second after convex grouping. The number of hypotheses generated by this algorithm is the second highest after the sliding window approach. This is due to the existence of various size craters, eroded craters, and craters located close to each other which makes it challenging to limit the range of the Hough transform parameters to lower the number of detections while keeping the recall rate high. As discussed in Section IV-D, large number of hypotheses generated by this algorithm are challenging noncrater regions which lower the precision of the HV step. Overall, we believe that the application of the Hough transform is practical for automatic crater detection in possibly less cratered sites, or when looking for specific size craters; alternatively, it can be used as a semiautomatic approach when manual verification of false detections is feasible.

The performance of the highlight-shadow region-based HG is summarized the fourth column of Table I. This algorithm is able to obtain a high recall rate of 98.49% by generating 436 hypotheses per image. The hypothesized crater detections IOU and the highest overlapping detections IOU were 45.08% and 59.38% with the ground truth, respectively.

The next column shows the performance of convex grouping. Although the differences with the rest of the algorithms are not significant, this algorithm seems to generate the most accurate hypotheses with a 54.1% average IOU with ground truth. Similarly, the highest overlapping hypotheses have an average IOU of 61.85% with the ground truth. Moreover, this algorithm produces the fewest hypotheses on average (i.e., 213 per image).

It should be emphasized that the convex grouping approach used here is significantly improved compared to the original approach used in [16]. In particular, the preprocessing step of removing large features from the original and negative images has allowed us to choose a lower gap tolerance (i.e., 25% from 49% used in [16]) and a higher saliency threshold (k) (i.e., 0.75 versus 0.51 used in [16], leading to less and higher quality groups. This has resulted in generating only 213 hypotheses on average per image compared to 7889 hypotheses per image in [16], while retaining similar recall rates.

TABLE I
PERFORMANCE OF HG ALGORITHMS ON TEST SET 2

	Sliding window	Hough Transform	Highlight shadow	Convex grouping	Interest points
Recall	99.61	99.61	98.49	98.44	99.22
Avg. IOU between GT and hypotheses	41.20 $\sigma = 11.13$	47.96 $\sigma = 15.79$	45.08 $\sigma = 13.34$	54.10 $\sigma = 13.72$	43.32 $\sigma = 12.12$
Avg. IOU between GT and the highest overlapping hypotheses	56.64 $\sigma = 10.07$	60.76 $\sigma = 12.92$	59.38 $\sigma = 13.52$	61.85 $\sigma = 12.85$	52.14 $\sigma = 12.48$
Avg. Number of Hypotheses	2813	773	436	213	298

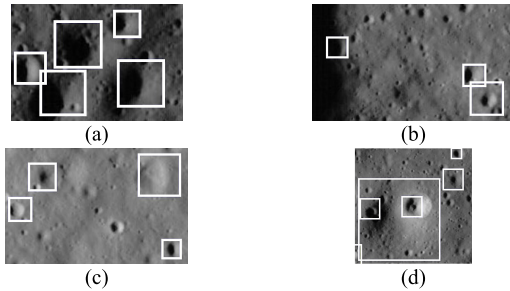


Fig. 4. Sample true hypotheses generated by (a) Hough transform, (b) highlight-shadow region, (c) convex grouping, and (d) interest points.

The last column of Table I summarizes the performance of using interest points for HG. As it can be observed, the overlap between the generated hypotheses and ground truth is lower than in the previous algorithms. However, this approach generates 298 hypotheses on average per image and ranks second after convex grouping. Most importantly, as discussed in Section IV-D, these hypotheses can be verified with high accuracy in HV which results in the best overall crater detection performance.

In conclusion, all the HG algorithms considered in this paper have been able in principle to detect craters with nearly perfect recall rate due to fine-tuning their parameters. A more meaningful analysis of their performance, however, can only be achieved in combination with the HV phase.

Fig. 4 demonstrates each HG approach by showing several sample hypotheses generated by each of them. For clarity, we only show the highest overlapping hypotheses with ground truth, while the rest of the hypotheses and the hypotheses corresponding to smaller craters which are not part of the ground truth have been removed. Specifically, Fig. 4(a) shows the successful detection of four craters in a high-density crater region using Hough transform. Fig. 4(b) demonstrates the success of the highlight-shadow region approach to detect a crater on the edge of a shaded part of the image with major parts of the crater rim not visible. Fig. 4(c) shows the strength of convex grouping in detecting two severely eroded craters. Finally, Fig. 4(d) shows a sample region where the interest points approach has detected two craters which are completely located inside another eroded crater.

D. HV Using CNNs

In our experiments, many CNN hyper parameters were tested on a validation set and the three CNNs discussed in

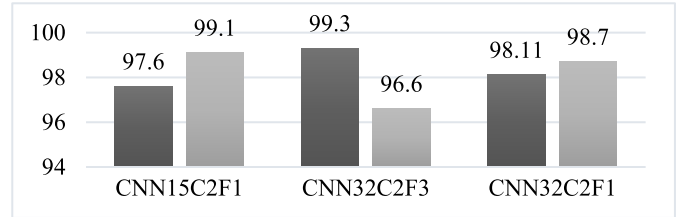


Fig. 5. Recall (dark gray) and precision (light gray) rates on Test Set 1 using CNNs trained on Training Set 1.

Section III-B were chosen as the best performing networks. In particular, various input image sizes were tested for each network. For instance, an input size of 32, instead of 15, for CNN₁₅C₂F₁ results in lower accuracy. Adding more convolutional or fully connected layers, or changing the activation functions did not result in performance improvements on the validation set. The three selected CNNs were trained using the backpropagation algorithm with a learning rate between 0.01 and 0.05 based on the validation set experiments. The intensity values of all training and test data fed to the CNNs were normalized in range -0.5 to $+0.5$.

In the first set of our HV experiments, the CNNs are trained on Training Set 1 and tested on Test Set 1. As shown in Fig. 5, due to the similarity between Training Set 1 and Test Set 1, all CNNs result in high accuracy. CNN₃₂C₂F₃ results in slightly higher recall rate but lower precision rate compared to the other CNNs. To perform a more meaningful comparison, we applied the CNNs on Test Set 2 in our next set of experiments

E. Performance Analysis by Combining HG With HV

Our goal in this set of experiments is to find the best performance on Test Set 2 using different combinations of HG and HV algorithms. We also investigate the effect of HG performance on the verification phase. In the first set of experiments, the hypotheses generated by each HG algorithm were verified using CNNs trained on Training Set 1. Table II summarizes the results of these experiments. Then, the same set of experiments are performed using CNNs trained on Training Set 2. Specifically, to apply a CNN on the hypotheses generated by a particular HG algorithm, the CNN is trained on a subset of Training Set 2 which is generated by the same HG algorithm. Table III summarizes the results of these experiments.

TABLE II
PERFORMANCE OF HV ON TEST SET 2 USING CNNs TRAINED ON TRAINING SET 1

	CNN ₁₅ C ₂ F ₁		CNN ₃₂ C ₂ F ₃		CNN ₃₂ C ₂ F ₁	
	Recall	Precision	Recall	Precision	Recall	Precision
Sliding window	84.49	63.18	87.59	58.7	88.75	71.78
Hough Transform	88.75	40.31	90.69	37.14	89.92	45.75
Highlight-shadow	84.49	50.58	94.18	47.83	93.79	60.80
Convex grouping	87.98	75.16	90.69	63.76	88.75	75.82
Interest points	81.78	93.77	89.14	92	84.55	96.78

TABLE III
PERFORMANCE OF HV ON TEST SET 2 USING CNNs TRAINED ON TRAINING SET 2

	CNN ₁₅ C ₂ F ₁		CNN ₃₂ C ₂ F ₃		CNN ₃₂ C ₂ F ₁	
	Recall	Precision	Recall	Precision	Recall	Precision
Hough Transform	91.47	62.59	93.41	48.1	92.12	54.34
Highlight-shadow	93.02	62.66	94.18	69.62	93.79	63.85
Convex grouping	90.11	75.38	92.24	66.66	89.53	78.30
Interest points	90.80	95.18	91.47	93.32	87.78	93.87

The main observation by comparing Tables II with III is that verification performance improves in general by employing Training Set 2. The first row of Table II shows the results of HV combined with the sliding window approach. The hypotheses generated by the sliding window approach are quite different from the ones generated by other HG approaches due to their similarity with Training Set 1 samples. As a result, HV accuracy is higher in this case. In particular, using sliding window-based HG, it is possible to get the highest recall rate of 88.75% and precision rate of 71.78% using CNN₃₂C₂F₁. The relative high precision rates compared to the next two rows of the table can be explained by the fact that unlike the hypotheses generated by the other algorithms, the majority of the hypotheses generated by the sliding window approach do not contain challenging geological features. In the case of the other HG algorithms, however, the extracted regions are typically more interesting containing geological features that are likely to be misclassified as crater leading to high false positive rates. The main drawback of the sliding window approach is the large number of hypotheses compared to the other HG methods (see Table I—row 4). Assuming that crater detection is applied on large planetary sites, this can be very problematic.

HV performance on hypotheses generated by the Hough transform, especially in terms of precision, is the lowest in Table II. Even CNN₃₂C₂F₁, which shows overall the best performance, has a recall rate of 89.92% and a precision rate of 45.75%. The main reason for this is the high number of challenging hypotheses generated by the Hough transform. Many of the hypothesized regions include geological features similar to craters which are not represented well in Training Set 1. As Table III shows, it is possible to improve the verification performance of all CNNs by training them on Training Set 2. In this case, an improved recall rate of 91.47% and precision rate of 62.59% is obtained for the Hough transform by CNN₁₅C₂F₁.

Similar observations can be made for HV combined with highlight-shadow detection approach. Assuming the CNNs trained on Training Set 1, the best verification performance

is obtained using CNN₃₂C₂F₁ (i.e., 93.79% and 60.8% recall and precision rates). As Table III shows, using Training Set 2 for training yields a recall rate of 94.18% and a precision rate of 69.62% for CNN₃₂C₂F₃.

Combining convex grouping with CNNs results in better performance compared to the previous methods as shown in Tables II and III. Among the CNNs trained on Training Set 1, CNN₃₂C₂F₁ has recall and precision rates of 88.75% and 75.82%; using Training Set 2, it is possible to improve these rates to 89.53% and 78.3%, respectively.

Considering precision rate alone, the best performance of 95.18% is obtained using interest point-based HG as shown in Table III. However, as it could be expected from the low IOU rates in Table I, the recall rates are relatively lower than the other algorithms in Tables II and III. While there is no clear best performing CNN in this case, the best recall rate of 91.47% is obtained using CNN₃₂C₂F₃ while the best precision rate of 95.18% is obtained using CNN₁₅C₂F₁.

Overall, Tables II and III show that verification performance using Hough transform and highlight-shadow HG is not satisfactory. This seems to be due to the fact that none of the training sets can properly represent the large number of challenging noncrater test samples. We believe, however, that using bootstrapping [16] to generate a more representative training set could improve verification results of all the algorithms discussed.

F. Further Discussion on the Experiments

To better understand the overall performance of each HG algorithm, we report in Fig. 6 the average recall and precision rates over all three CNNs. Our results indicate that regardless of the training data set used, verification of hypotheses generated by the interest points approach yields the best performance with convex grouping ranking second. Therefore, we believe that HG using interest points or convex grouping combined with CNN-based HV is the most promising crater detection strategy. Fig. 7 shows some examples based on these two approaches. The hypotheses generated by convex grouping

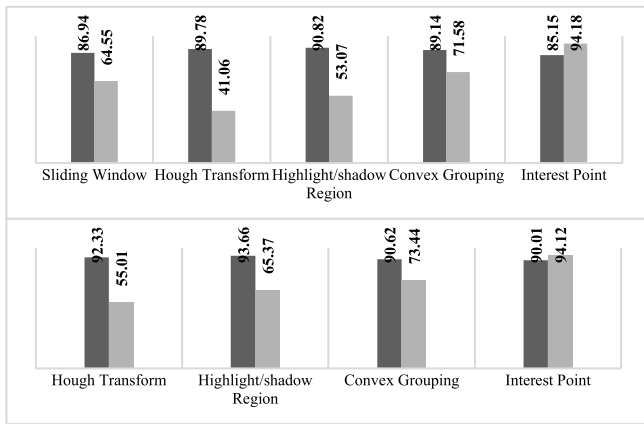


Fig. 6. Average recall (dark gray) and precision (light gray) rates of HV, categorized by the HG algorithm, using CNNs trained on (Top) Training Set 1 and (Bottom) Training Set 2.

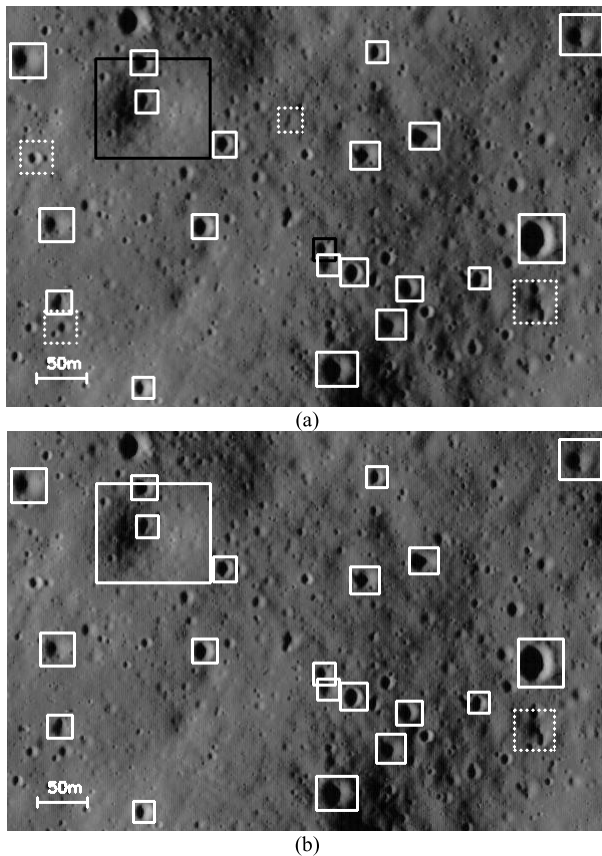


Fig. 7. Crater detection results using (a) convex grouping-based HG combined with CNN₃₂C₂F₁ for HV and (b) interest point-based HG combined with CNN₁₅C₂F₁ for HV. True positives, false positives, and false negatives are shown in solid white, dotted white, and solid black, respectively

are verified by CNN₃₂C₂F₁ [Fig. 7(a)] while CNN₁₅C₂F₁ is applied to verify the hypotheses generated by the interest points [Fig. 7(b)]. Both CNNs are trained on Training Set 2. It should be noted that since only craters with a radius larger than 10 m are considered in our evaluations, smaller craters are not marked in the figure.

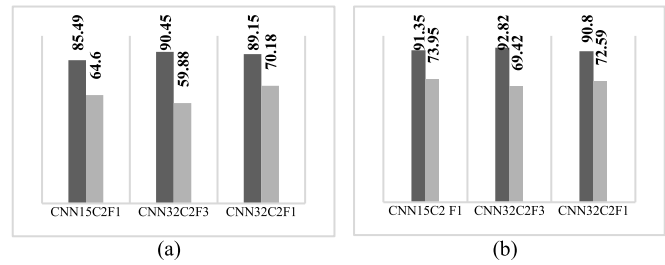


Fig. 8. Average recall (dark gray) and precision (light gray) rates on Test Set 2 using CNNs trained on (a) Training Set 1 and (b) Training Set 2.

In evaluating different CNN architectures, Table II shows that CNN₃₂C₂F₁ outperforms the other two networks assuming three different HG algorithms, namely, sliding window, Hough transform, and highlight shadow. Also in the verification of hypotheses generated by convex grouping, CNN₃₂C₂F₁ and CNN₁₅C₂F₁ produce very similar results. Finally, CNN₃₂C₂F₃ shows the most satisfactory performance using highlight-shadow and interest point-based HG algorithms, although the other two networks produce better precision rates. Fig. 8(a) shows the performance of each CNN averaged over all HG algorithms. Although averaging the rates in Table II is not very accurate due to different numbers of hypotheses generated by each HG algorithm, it still demonstrates the superiority of CNN₃₂C₂F₁ compared to the other CNNs. It should be reminded that the positive and negative samples in Training Set 1 are generated from random locations around cratered and noncratered regions of the images, but the hypotheses generated by the HG algorithms (except for the sliding window) have different characteristics. Therefore, the performance analysis of CNNs trained on Training Set 1, and tested on hypotheses generated by HG algorithms implies CNN₃₂C₂F₁ generalizes better than the other two networks.

Unlike Table II results, analyzing Table III results from HV perspective does not show that any of the CNNs is superior to the others. In particular, CNN₁₅C₂F₁ performs the best when combined with Hough transform, while CNN₃₂C₂F₃ shows the best performance when combined with the highlight-shadow HG approach. Both networks perform very well when applied on interest point-based HG. In the case of hypotheses generated by convex grouping, CNN₁₅C₂F₁ and CNN₃₂C₂F₁ perform relatively better than CNN₃₂C₂F₃. Considering average verification performance, however, CNN₁₅C₂F₁ performs slightly better than the other networks [Fig. 8(b)]. Regardless of average HV performance, the results of Table III show which combination of HV and HG algorithms should be used to obtain the best performance when training data similar the test site is available.

Last but not least, it should be mentioned that a number of false positives reported in our experiments are detected close to ground truth craters but with an overlap less than 30% with them. As shown in Fig. 7(a), this is especially the case when using convex grouping for HG. By manually removing such detections from the false positives, the precision rate of convex grouping-based HG and CNN₃₂C₂F₁-based HV can improve

to 92.4%. The same modification results in 97.9% precision for interest point-based HG and CNN₁₅C₂F₁-based HV.

V. CONCLUSION

Crater detection is an important task in planetary sciences with major applications in space exploration and research. In this paper, we investigated a two-step approach for automatic crater detection based on HG and HV. Specifically, four unsupervised algorithms were considered for detecting possible crater regions: Hough transform, highlight-shadow region detection, convex grouping, and interest points detection. A sliding window approach was also considered for comparison. Through comprehensive experiments, we investigated the performance of the HG algorithms in combination with CNNs for HV. Our experimental results provide valuable insights about the best combinations and the importance of the training data on performance. Overall, the best HG algorithms were based on interest points detection and convex grouping in combination with CNNs for HV. It should be mentioned that among the HG methods tested, only the convex grouping method could provide a more accurate measure of the size of the craters detected. This is because it encloses the detected craters by a convex group of lines although the detections are shown by the largest rectangle that encloses a convex group. Depending on the application in mind, reporting crater size information could be very important.

For future work, we plan to extend our methods in order to detect smaller size craters (i.e., less than 10-m radius). The main reason for limiting our work to craters within a specific size range (i.e., 10–100 m), was the availability of ground truth in that range. Although we have not performed systematic experiments to detect smaller size craters, preliminary results using our interest point-based CDA have shown that it is possible to detect smaller craters with good accuracy mainly because smaller craters form fairly compact clusters of interest points. We also plan to analyze the performance of our algorithms with respect to accurate crater localization and sizing. Fusing hypotheses generated by different HG techniques to further improve performance is also a topic for future research. Although such an approach will increase computational cost, we expect improved recall and precision rates due to different characteristics of the HG approaches.

Moreover, we plan to study the problem of crater detection assuming limited training data. In particular, using our trained CNNs on lunar images and transfer learning approaches, we intend to test our algorithms on data from other planets. We also plan to enhance overall crater detection accuracy using DEM. In particular, we plan to investigate the performance hybrid CDAs which combine information both from optical images and DEMs. By improving the resolution of planetary DEMs using super resolution techniques, it might be possible to apply our best performing CDAs based on interest point detection or convex grouping to DEMs with few modifications.

REFERENCES

- [1] N. G. Barlow, "Constraining geologic properties and processes through the use of impact craters," *Geomorphology*, vol. 240, pp. 18–33, Jul. 2015.
- [2] W. K. Hartmann and G. Neukum, "Cratering chronology and the evolution of Mars," *Space Sci. Rev.*, vol. 96, pp. 165–194, Apr. 2001.
- [3] G. Salamunićar and S. Lončarić, "Open framework for objective evaluation of crater detection algorithms with first test-field subsystem based on MOLA data," *Adv. Space Res.*, vol. 42, no. 1, pp. 6–19, 2008.
- [4] M. Yu, H. Cui, and Y. Tian, "A new approach based on crater detection and matching for visual navigation in planetary landing," *Adv. Space Res.*, vol. 53, no. 12, pp. 1810–1821, 2014.
- [5] T. F. Stepinski, W. Ding, and R. Vilalta, "Detecting impact craters in planetary images using machine learning," *Intelligent Data Analysis for Real-Life Applications: Theory and Practice*, PA, USA: IGI Global, 2012, pp. 146–159. [Online]. Available: <https://www.igi-global.com/chapter/detecting-impact-craters-planetary-images/67447>
- [6] G. Salamunićar, S. Lončarić, P. Pina, L. Bandeira, and J. Saraiva, "MA130301GT catalogue of Martian impact craters and advanced evaluation of crater detection algorithms using diverse topography and image datasets," *Planet. Space Sci.*, vol. 59, no. 1, pp. 111–131, 2011.
- [7] G. Salamunićar, S. Lončarić, and E. Mazarico, "LU60645GT and MA132843GT catalogues of Lunar and Martian impact craters developed using a Crater Shape-based interpolation crater detection algorithm for topography data," *Planet. Space Sci.*, vol. 60, no. 1, pp. 236–247, 2012.
- [8] G. Salamunićar, S. Lončarić, P. Pina, L. Bandeira, and J. Saraiva, "Integrated method for crater detection from topography and optical images and the new PH9224GT catalogue of Phobos impact craters," *Adv. Space Res.*, vol. 53, no. 12, pp. 1798–1809, 2014.
- [9] G. Salamunićar, S. Lončarić, A. Grumpe, and C. Wöhler, "Hybrid method for crater detection based on topography reconstruction from optical images and the new LU78287GT catalogue of Lunar impact craters," *Adv. Space Res.*, vol. 53, no. 12, pp. 1783–1797, 2014.
- [10] R. M. Z. Sun and G. Bebis, "Monocular precrash vehicle detection: Features and classifiers," *IEEE Trans. Image Process.*, vol. 15, no. 7, pp. 2019–2034, Sep. 2006.
- [11] H. Yuen, J. Princen, J. Illingworth, and J. Kittler, "Comparative study of Hough Transform methods for circle finding," *Image Vis. Comput.*, vol. 8, no. 1, pp. 71–77, 1990.
- [12] E. R. Urbach and T. F. Stepinski, "Automatic detection of sub-km craters in high resolution planetary images," *Planet Space Sci.*, vol. 57, no. 7, pp. 880–887, Jun. 2009.
- [13] D. W. Jacobs, "Robust and efficient detection of salient convex groups," *IEEE Trans. Pattern Anal. Mach. Intell.*, vol. 18, no. 1, pp. 23–37, Jan. 1996.
- [14] J. Shi and C. Tomasi, "Good features to track," in *Proc. IEEE Conf. Comput. Vis. Pattern Recognit.*, Seattle, WA, USA, Jun. 1994, pp. 593–600.
- [15] Challenge for NASA Tournament Lab. *Crater Detection*. Accessed: Jan. 15, 2016. [Online]. Available: <https://ti.arc.nasa.gov/news/crater-detection-challenge/>
- [16] E. Emami, G. Bebis, A. Nefian, and T. Fong, "Automatic crater detection using convex grouping and convolutional neural networks," in *Proc. 11th Int. Symp. Vis. Comput.*, Las Vegas, NV, USA, 2015, pp. 213–224.
- [17] G. Troglia, J. Le. Moigne, J. A. Benediktsson, G. Moser, and S. B. Serpico, "Automatic extraction of ellipsoidal features for planetary image registration," *IEEE Geosci. Remote Sens. Lett.*, vol. 9, no. 1, pp. 95–99, Jan. 2012.
- [18] M. J. Galloway, G. K. Benedix, P. A. Bland, J. Paxman, M. C. Towner, and T. Tan, "Automated crater detection and counting using the Hough transform," in *Proc. IEEE Int. Conf. Image Process.*, Paris, France, Oct. 2014, pp. 1579–1583.
- [19] B. D. Bue and T. F. Stepinski, "Machine detection of martian impact craters from Digital Topography Data," *IEEE Trans. Geosci. Remote Sens.*, vol. 45, no. 1, pp. 265–274, Jan. 2007.
- [20] R. Honda, O. Konishi, R. Azuma, H. Yokogawa, S. Yamanaka, and Y. Iijima, "DaData mining system for planetary images-crater detection and categorization," in *Proc. Int. Workshop Mach. Learn. Spatial Knowl. Conjoint. (ICML)*, Stanford, CA, USA, 2000, pp. 103–108.
- [21] G. Salamunićar and S. Lončarić, "Method for crater detection from martian digital topography data using gradient value/orientation, morphology, vote analysis, slip tuning, and calibration," *IEEE Trans. Geosci. Remote Sens.*, vol. 48, no. 5, pp. 2317–2329, May 2010.
- [22] B. Leroy, G. Medioni, E. Johnson, and L. Matthies, "Crater detection for autonomous landing on asteroids," *Image Vis. Comput.*, vol. 19, no. 11, pp. 787–792, 2001.
- [23] L. Bandeira, J. Saraiva, and P. Pina, "Impact crater recognition on Mars based on a probability volume created by template matching," *IEEE Trans. Geosci. Remote Sens.*, vol. 45, no. 12, pp. 4008–4015, Dec. 2007.

- [24] A. A. Smirnov, "Exploratory study of automated crater detection algorithm," Boulder, CO, USA, Tech. Rep., 2012. [Online]. Available: <http://citeseerx.ist.psu.edu/viewdoc/download?doi=10.1.1.138.8321&rep=rep1&type=pdf>
- [25] T. F. Stepinski, M. P. Mendenhall, and B. D. Bue, "Machine cataloging of impact craters on Mars," *Icarus*, vol. 203, no. 1, pp. 77–87, 2009.
- [26] R. Savage *et al.*, "A Bayesian approach to subkilometer crater shape analysis using individual HiRISE images," *IEEE Trans. Geosci. Remote Sens.*, vol. 56, no. 10, pp. 5802–5812, Oct. 2018.
- [27] A. Liu, M. Chen, and W. Pan, "Crater detection algorithm with part PHOG features for safe landing," in *Proc. Int. Conf. Syst. Inform.*, May 2012, pp. 103–106.
- [28] R. Martins, P. Pina, J. S. Marques, M. Silveira, and M. Silveira, "Crater detection by a boosting approach," *IEEE Geosci. Remote Sens. Lett.*, vol. 6, no. 1, pp. 127–131, Jan. 2009.
- [29] S. Jin and T. Zhang, "Automatic detection of impact craters on Mars using a modified adaboosting method," *Planetary Space Sci.*, vol. 99, pp. 112–117, Sep. 2014.
- [30] E. Emami, G. Bebis, A. Nefian, and T. Fong, "On crater verification using mislocalized crater regions," in *Proc. IEEE Winter Conf. Appl. Comput. Vis. (WACV)*, Santa Rosa, CA, USA, Mar. 2017, pp. 1098–1104.
- [31] J. Cohen *et al.*, "Crater detection via convolutional neural networks," in *Proc. 47th Lunar Planetary Sci. Conf.*, Houston, TX, USA, 2016.
- [32] L. F. Palafox, C. W. Hamilton, S. P. Scheidt, and A. M. Alvarez, "Automated detection of geological landforms on Mars using convolutional neural networks," *Comput. Geosci.*, vol. 101, pp. 48–56, Apr. 2017. [Online]. Available: <https://www.hou.usra.edu/meetings/lpsc2016/pdf/1143.pdf>
- [33] T. Pavlidis and S. L. Horowitz, "Segmentation of plane curves," *IEEE Trans. Comput.*, vol. 100, no. 8, pp. 860–870, Aug. 1974.
- [34] M. Ding, Y. Cao, and Q. Wu, "Novel approach of crater detection by crater candidate region selection and matrix-pattern-oriented least squares support vector machine," *Chin. J. Aeronaut.*, vol. 26, no. 2, pp. 385–393, Apr. 2013.
- [35] Y. Lecun, L. Bottou, Y. Bengio, and P. Haffner, "Gradient-based learning applied to document recognition," *Proc. IEEE*, vol. 86, no. 11, pp. 2278–2324, Nov. 1998.



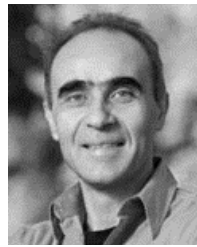
Ebrahim Emami received the B.Sc. degree in computer engineering from the University of Kerman, Kerman, Iran, in 2009, and the M.Sc. degree in computer engineering (artificial intelligence) from the Iran University of Science and Technology, Tehran, Iran, in 2012. He is currently pursuing the Ph.D. degree in computer science and engineering with the University of Nevada, Reno, Reno, NV, USA.

His research interests include machine learning, computer vision, and deep learning.



Touqeer Ahmad received the B.S. degree in computer engineering from NUCES-FAST, Lahore, Pakistan, in 2008, the M.Sc. degree in computer science from the University of York, York, U.K., in 2011, and the M.S. degree in computer science and engineering and the Ph.D. degree in computer science and engineering from the University of Nevada, Reno, NV, USA, in 2014 and 2017, respectively.

He is currently a Computer Vision Engineer with Blackmagic Design, Colorado Springs, CO, USA. His research interests include applied machine learning, computer vision, and deep learning specifically for image restoration problems.



George Bebis received the B.S. degree in mathematics and the M.S. degree in computer science from the University of Crete, Crete, Greece, in 1987 and 1991, respectively, and the Ph.D. degree in electrical and computer engineering from the University of Central Florida, Orlando, FL, USA, in 1996.

He is currently a Foundation Professor with the Department of Computer Science and Engineering (CSE), University of Nevada, Reno (UNR), Reno, NV, USA, and the Director of the Computer Vision Laboratory. From 2013 to 2018, he served as a Department Chair of CSE, UNR. His research has been funded by NSF, NASA, ONR, NIJ, and Ford Motor Company. His research interests include computer vision, image processing, pattern recognition, machine learning, and evolutionary computing.

Dr. Bebis is an Associate Editor of the *Machine Vision and Applications Journal* and serves on the Editorial Board of the *International Journal on Artificial Intelligence Tools*, the *Pattern Analysis and Applications*, and the *Computer Methods in Biomechanics and Biomedical Engineering: Imaging and Visualization*. He has served on the program committees of various national and international conferences and the Founder/main Organizer of the International Symposium on Visual Computing.



Ara Nefian received the B.S. degree from Politehnica University Bucharest, Bucharest, Romania, in 1993, and the MSEE and Ph.D. degrees from the Georgia Institute of Technology, Atlanta, GA, USA, in 1999.

He led the Lunar Mapping and Modeling from Apollo era imagery and was the Principal Investigator for the Lunar Albedo Reconstruction project. In 2005, he was a part of the Computer Vision Group within the Stanford Racing Team (Stanley) that won the DARPA Autonomous

Navigation Grand Challenge. Since 2012, he led the Rover Navigation Team in supporting NASA future robotics Lunar mission and is a collaborator on the Science Team for Mars Curiosity rover mission. He is currently a Senior Scientist with SGT, NASA Ames Research Center, Moffett Field, CA, USA. He has co-authored over 100 research papers and holds ten U.S. and international patents. His research interests include the areas of computer vision, machine learning, and robotics.



Terry Fong received the B.S. and M.S. degrees in aeronautics and astronautics from the Massachusetts Institute of Technology, Cambridge, MA, USA, and the Ph.D. degree in robotics from Carnegie Mellon University, Pittsburgh, PA, USA.

He was the Deputy Leader of the Virtual Reality and Active Interfaces Group with the Swiss Federal Institute of Technology, Lausanne, Switzerland. He is currently a Senior Scientist of autonomous systems with NASA and the Chief Roboticist of the NASA Ames Intelligent Robotics Group, Moffett Field, CA, USA.